Unique Cluster-Support Effect of a Co$_3$O$_4$/TiO$_2$-3DHS Nanoreactor for Efficient Plasma-Catalytic Oxidation Performance

Yujie Liao, Kun Zhao, Ke Chen, Chenghua Sun, and Dong Fu*

Read Online

| ACCESS | | Metrics & More | | Article Recommendations | | Supporting Information |

ABSTRACT: For environmental catalysis, a central topic is the design of high-performance catalysts and advanced mechanism studies. In the case of the removal of flue gas pollutants from coal-fired power plants, highly selective nanoreactors have been widely utilized together with plasma discharge characteristics, such as the catalytic oxidation of NO. Herein, a novel reactor with a three-dimensional hollow structure of TiO$_2$ confining Co$_3$O$_4$ nanoclusters (Co$_3$O$_4$/TiO$_2$-3DHS) has been developed for plasma-catalytic oxidation of NO, whose performance was compared with that of the commercial TiO$_2$ confining Co$_3$O$_4$ cluster (Co$_3$O$_4$/TiO$_2$). Specifically, Co$_3$O$_4$/TiO$_2$-3DHS presented a higher efficiency (almost 100%) within lower peak−peak voltage (V_{P-P}). More importantly, the NO oxidation efficiency was between 91.5 and 94.5% after a long time of testing, indicating that Co$_3$O$_4$/TiO$_2$-3DHS exhibits more robust sulfur and water tolerance. Density functional theory calculations revealed that such impressive performance originates from the unique cluster-support effect, which changes the distribution of the active sites on the catalyst surface, resulting in the selective adsorption of flue gas. This investigation provides a new strategy for constructing a three-dimensional hollow nanoreactor for the plasma-catalytic process.
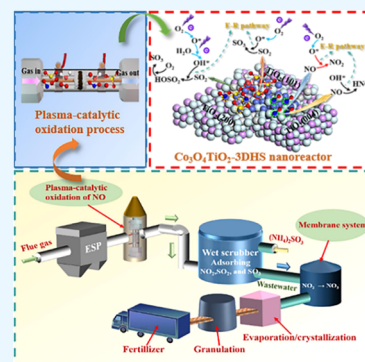
1. INTRODUCTION

Human health and global environmental protection underline the need to design efficient and environmentally friendly industrial flue gas control systems.[1] As far as flue gas denitrification is concerned, the traditional selective catalytic reduction (SCR) technology has been extensively applied,[2−4] while its capacity to remove nitric oxide (NO) from flue gas is far from ideal due to conflicting redox effects.[5] Under such a context, catalytic oxidation of NO has emerged as a promising approach due to its flexibility, controllability, and wide applicability.[6] Among various NO oxidation methods, non-thermal plasma (NTP) technology, highlighted by its rapid thermodynamics at low temperatures, has attracted much attention. An et al.[7] loaded a series of Co-Mn/Ti catalysts into the discharge region of a dielectric barrier discharge (DBD) reactor for NO catalytic oxidation experiments. The results revealed that the combination of DBD and Co-Mn/Ti catalysts exhibited excellent NO oxidation performance, achieving a rate of 91.3%, surpassing that of the DBD process alone. Wang et al.[8] utilized a MnO$_X$ catalyst in a DBD reactor to investigate NO conversion. The experimental findings demonstrated that plasma discharge augmented the chemisorbed oxygen concentration on the surface of the catalyst. Furthermore, a partial transformation of the manganese valence state from trivalent to tetravalent was identified, contributing to the enhanced oxidation in the plasma-catalytic system.

So far, NTP technology needs to address two main challenges before industry-level flue gas denitrification, namely,

catalyst poisoning associated with the coexistence of SO$_2$ and H$_2$O and discharge efficiency, as determined by the synergistic effect between the catalyst and the plasma, both of which underline the significance of the rational design of advanced catalysts. Transition metals manifest a diverse range of valence states, while their oxides demonstrate pronounced redox capabilities, thereby establishing them as a ubiquitous option for the fabrication of catalysts.[9,10] Owing to its abundance, low cost, chemical stability, and resistance to acids and bases, titanium dioxide (TiO$_2$) is a commonly employed synthetic material in the manufacture of commercial catalysts.[11,12] In the literature, the combination of transition-metal oxides as active components and TiO$_2$ as a support has been well demonstrated as high-performance catalysts for NO removal under the NTP scheme.[13−15] So far, extensive efforts have been made in the screening of transition-metal active components, from the optimization of active components to delicate engineering of favorable hollow structures,[4,16] such as the combination of three-dimensional hollow geometries of TiO$_2$ coupled with Fe$_1$/TiO$_2$ microspheres and Pd@TiO$_2$@ZnIn$_2$S$_4$ nanobox.[17,18] As demonstrated by these studies, the

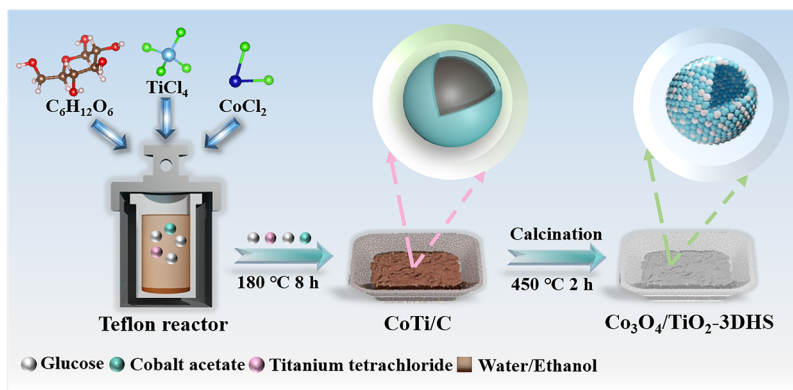**Figure 1.** Schematic illustration showing the fabrication strategy of the Co_3O_4/TiO_2-3DHS catalyst.

key value of the confinement effect associated with hollow nanoreactors has been well established, such as the impact on the electronic and geometric structure of active sites, which plays an essential role in charge transfer and separation.[4,6,19]

Based on the above considerations, the main purpose of this investigation is to study the performance of catalysts with different structures for NO oxidation in a dielectric barrier discharge (DBD) reactor to understand the advantages of a three-dimensional hollow structure (3DHS) in the plasma-catalytic process. Based on our previous experiments (Figure S1, Supporting Information) and investigation, cobalt oxide was chosen as the active component, and TiO_2 was selected as the support. The Co_3O_4/TiO_2 and Co_3O_4/TiO_2-3DHS catalysts were prepared by wet impregnation and hydrothermal methods, respectively. In addition, the influence of coexisting SO_2 and H_2O on the plasma-catalytic oxidation performance of NO was compared under the condition of 21−31 kV. The experiment results showed that the Co_3O_4/TiO_2-3DHS catalysts exhibit higher oxidation efficiency, higher discharge efficiency, and more excellent sulfur/water tolerance. The density functional theory (DFT) calculations revealed that the three-dimensional hollow structure has a unique cluster-support effect, driving the selective adsorption of flue gas on the catalyst surface and weakening the catalyst poisoning effect. This work provides a new strategy for the efficient oxidation of NO in the plasma-catalytic process.

2. EXPERIMENTAL SECTION

2.1. Catalyst Preparation. In this work, we synthesized two different structures catalysts (Co_3O_4/TiO_2-3DHS and Co_3O_4/TiO_2) by hydrothermal method and wet impregnation method, respectively. A typical hydrothermal synthesis process is described as follows: 0.2 mL of pure $TiCl_4$ (AR grade, McLean Biochemical Co., Ltd.) was slowly added into 55.0 mL of ice-cold deionized water to form a $TiCl_4$ aqueous solution, and then glucose powder (2.7 g, AR grade, McLean Biochemical Co., Ltd.) and an appropriate amount of metal salts (0.4 g $CoCl_2 \cdot 6H_2O$, metals basis, McLean Biochemical Co., Ltd.) were dispersed in a mixed solution made up of ethanol (4 mL, AR grade, Huikang Chemical Technology Co., Ltd.), deionized water (55.0 mL), and $TiCl_4$ aqueous solution with the aid of ultrasonication for 10 min. Subsequently, the resulting suspension was filled in a Teflon autoclave at 180 °C for 8 h. The obtained precursor was collected into a centrifuge tube, and the centrifuge tube was washed with deionized water and ethanol six times and then dried at 70 °C for 12 h. The

composite samples were calcined at 450 °C in the air for 2 h and then cooled naturally to get the three-dimensional Co_3O_4/TiO_2-3DHS catalyst. A schematic diagram of the Co_3O_4/TiO_2-3DHS synthesis process is illustrated in Figure 1. The synthesis method of Co_3O_4/TiO_2 is illustrated in the Supporting Information.

2.2. Catalyst Characterization. X-ray diffraction (XRD) patterns were obtained on an X-ray diffractometer (D8, Bruker, Germany) with Cu Kα radiation (λ = 0.1542 nm). The step-scans were taken over the 2θ range of 10−80°. Crystallographic information was obtained comparing XRD patterns to the Joint Committee on Powder Diffraction Standards (JCPDS).

The morphologies of the catalysts were characterized by transmission electron microscopy (TEM) measurements using a JEM-2100F TEM model. X-ray photoelectron spectroscopy (XPS) data were analyzed with an Escalab 250Xi electron spectrometer (Thermo Scientific Company). The binding energy was calibration based on the C 1s peak at 284.8 eV.

The distinctive physicochemical properties of catalysts were analyzed by the Brunauer−Emmett−Teller (BET) method using the Micromeritics adsorption equipment (ASAP2420). To calculate the specific surface area, N_2 adsorption and desorption isotherms were used, which were recorded using the Brunauer−Emmett−Teller method. Fourier transform infrared (FTIR) spectra were recorded with a spectrometer (Thermo Nicolet iS5) in the transmission mode.

2.3. Experimental Steps. The main components of the experimental NO oxidation platform are a gas distribution system, a DBD reactor, and a gas analysis system (Figure S2, Supporting Information).[20] In brief, a quartz tube with an inner diameter of 20 mm and an outer diameter of 25 mm served as a dielectric layer. A grounded stainless steel mesh with a length of 45 mm was used as the outer electrode, wrapped around the external surfaces of the quartz tube. A stainless steel rod with a diameter of 16 mm and a length of 265 mm was used as the high-voltage electrode and placed in the axis of the inner quartz tube.[21,22] The length of the discharge region was fixed at 45 mm with a discharge gap of 4 mm. In the plasma-catalytic reaction experiment, a certain amount of catalysts are used to fill the discharge gap between the internal electrode and the quartz tube. The DBD reactor was connected to an alternating current (AC) high-voltage power supply with a variable peak voltage at a fixed frequency of 10 kHz. Electrical signals were sampled by a digital oscilloscope (DPO2012B, Tektronix).
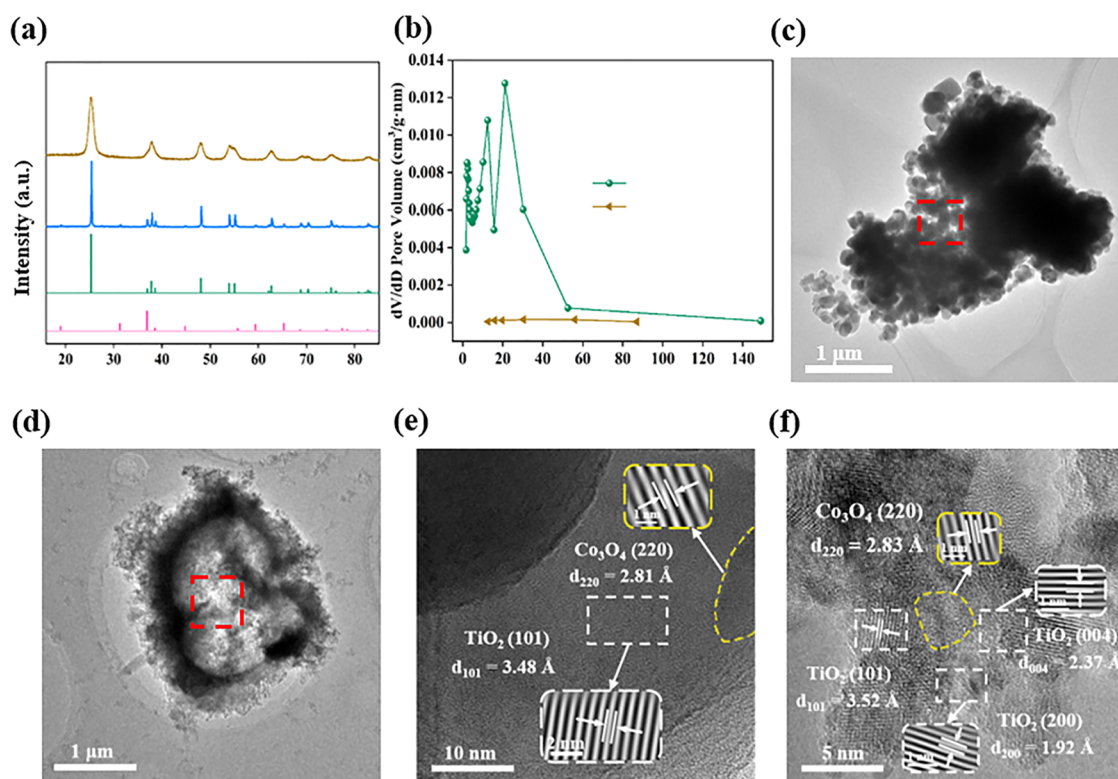
Figure 2. (a) XRD patterns of the fresh catalysts. (b) Pore size distribution of the fresh catalysts. (c, d) TEM micrographs of Co_3O_4/TiO_2 and Co_3O_4/TiO_2-3DHS, respectively. (e, f) HRTEM micrograph of Co_3O_4/TiO_2 and Co_3O_4/TiO_2-3DHS, respectively.

For performance tests, a mixture of N_2, O_2 (6 vol %), NO (160 ppm), SO_2 (400 ppm), and H_2O (5 vol %) was supplied to the reactor at a constant flow rate of 2.2 L min^{-1}. A flue gas analyzer (J2KN, Rbr Analytical Technologies Ltd., Germany) was used to monitor and record the concentration of reacted NO. NO oxidation efficiency and SO_2 conversion efficiency in the plasma catalysis system have been determined by eqs 1 and 2

$$\eta_{NO} = \frac{C_{NO,in} - C_{NO,out}}{C_{NO,in}} \times 100\% \tag{1}$$

$$\eta_{SO_2} = \frac{C_{SO_2,in} - C_{SO_2,out}}{C_{SO_2,in}} \times 100\% \tag{2}$$

2.4. Computational Calculations. Density functional theory (DFT) calculations were conducted using the Perdew−Burke−Ernzerhof (PBE) functional and projector augmented wave (PAW) basis set, as embedded by Vienna Ab initio Simulation Package (VASP) software.[23,24] Three slab models ($Co_3O_4/TiO_2(101)$, $Co_3O_4/TiO_2(200)$, $Co_3O_4/TiO_2(004)$) were constructed using (101), (200), and (004) planes of TiO_2 and (220) plane of Co_3O_4 cluster, as identified by high-resolution TEM (HRTEM) images in Figure S3 (Supporting Information), while the vacuum layer thickness was set at 15 Å. The electron−electron exchange and correlation were calculated using generalized gradient approximation plus the Hubbard model (GGA + U). The U_{eff} of Ti and Co was set to 4.0 and 3.4 eV, respectively.[25] A kinetic energy cutoff of 450 eV was applied. Moreover, a $1 \times 1 \times 1$ Monkhorst−Pack k-point grid was used for the calculation of geometry structures. The structural optimization reaches convergence when the energy

difference drops below 10^{-5} eV and the force difference falls below 0.02 eV/Å.[23,26,27]

The binding energy (E_{bind}) of the Co_3O_4 catalyst has been calculated as follows:

$$E_{bind} = E_{Co_3O_4/TiO_2} - E_{TiO_2} - E_{Co_3O_4} \tag{3}$$

where $E_{Co_3O_4/TiO_2}$, E_{TiO_2} and $E_{Co_3O_4}$ represent the calculated energy of Co_3O_4/TiO_2, TiO_2 substrate, and Co_3O_4 cluster.

The gas-adsorption energy (E_{ads}) has been calculated as follows

$$E_{ads} = E_{gas/sys} - E_{sys} - E_{gas} \tag{4}$$

where $E_{gas/sys}$, E_{sys}, and E_{gas} represent the total energies of gas/Co_3O_4/TiO_2, Co_3O_4/TiO_2 system, and single gas molecules (NO, H_2O, SO_2), under which negative E_{ad} indicates stable adsorption.

3. RESULTS AND DISCUSSION

3.1. Structure and Morphology Identification. To determine the structures of Co_3O_4/TiO_2 and Co_3O_4/TiO_2-3DHS, the composites were characterized by XRD. As illustrated in Figure 2a, the characteristic peaks of anatase TiO_2 belonging to the tetragonal crystal system (JCPDS 99-0008) were detected as the main phase in the two catalysts. Additionally, The weak characteristic peaks of Co_3O_4, belonging to the cubic crystal system (JCPDS 78-1969), were detected in the Co_3O_4/TiO_2 catalyst. No significant characteristic peaks of Co_3O_4 were detected in the Co_3O_4/TiO_2-3DHS catalyst, indicating that the dispersion of cobalt oxides in the Co_3O_4/TiO_2-3DHS prepared by the hydro-thermal method was higher. In addition, the phase sizes calculated by the Scherrer formula are listed in Table S1
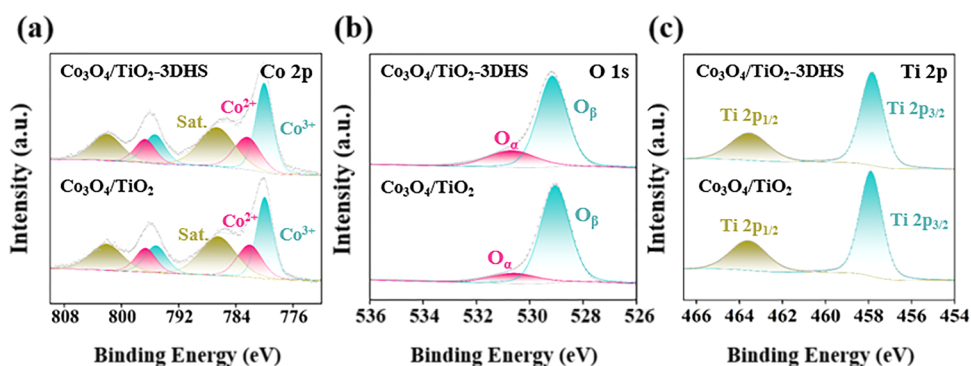
Figure 3. High-resolution XPS survey of Co_3O_4/TiO_2 and Co_3O_4/TiO_2-3DHS: (a) Co 2p, (b) O 1s, and (c) Ti 2p.
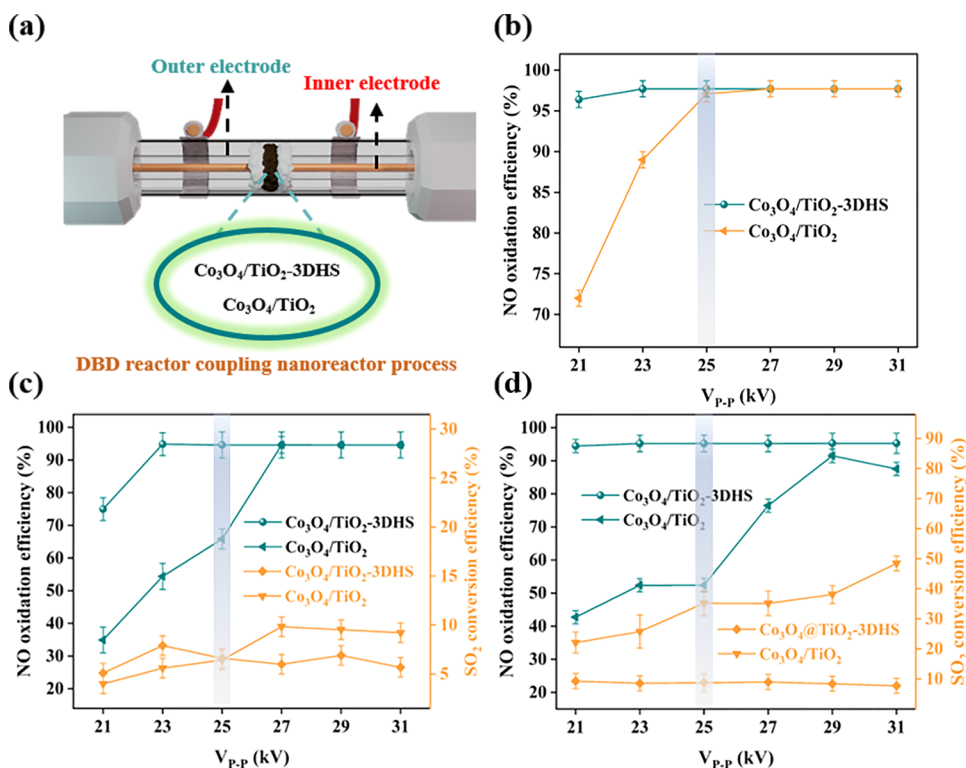

Figure 4. (a) Schematic diagram of catalyst filling. (b) NO oxidation efficiency under plasma catalysis conditions without SO_2 and H_2O. (c) NO oxidation efficiency under plasma catalysis conditions with SO_2. (d) NO oxidation efficiency under plasma catalysis conditions with SO_2 and H_2O. NO: 160 ppm; SO_2: 400 ppm; O_2: 6 vol %; and H_2O: 5 vol %.

(Supporting Information), and the sizes of Co_3O_4/TiO_2 and Co_3O_4/TiO_2-3DHS are 56.8 and 7.7 nm, respectively.[28] Furthermore, Figure 2b shows the pore size distribution for all materials, from which a smaller average pore size was observed for Co_3O_4/TiO_2-3DHS as compared to that of Co_3O_4/TiO_2.

Textural properties are listed in Table S1 (Supporting Information), according to which the Co_3O_4/TiO_2 showed a specific surface area of 4.65 $m^2 \cdot g^{-1}$, with a pore volume of 0.06 $cm^3 \cdot g^{-1}$, respectively. However, the specific surface area and pore volume of the Co_3O_4/TiO_2-3DHS catalyst increased to 89.76 $m^2 \cdot g^{-1}$ and 0.43 $cm^3 \cdot g^{-1}$, respectively. To further examine the microstructure and morphology of the two Co_3O_4/TiO_2 and Co_3O_4/TiO_2-3DHS catalysts, the samples were characterized by TEM, as presented in Figure 2c,d. It is observed that Co_3O_4/TiO_2 has an agglomeration structure attributed to the accumulation of a significant amount of particles, while Co_3O_4/TiO_2-3DHS shows a three-dimensional

hollow structure. High-resolution TEM (HRTEM) gives the d-spacing of the Co_3O_4/TiO_2 and Co_3O_4/TiO_2-3DHS (yellow and white colors indicate the Co_3O_4 and TiO_2 lattices, respectively). Figure 2e shows the high-resolution lattice fringes of the Co_3O_4/TiO_2; the fringes with d-spacings of 3.48 and 2.81 Å correspond to the (101) plane in TiO_2 and (220) plane in Co_3O_4 cluster, respectively. The high-resolution lattice fringes of the Co_3O_4/TiO_2-3DHS are plotted in Figure 2f: the fringes with d-spacings of 3.52, 2.37, and 1.92 Å correspond to the (101), (004), and (200) planes in TiO_2, respectively; the lattice spacing of 2.83 Å was ascribed to the (220) plane in Co_3O_4 cluster. Concerning typical TiO_2 substrate, a key difference brought by TiO_2-3DHS is that the Co_3O_4 cluster was surrounded by multiple TiO_2 planes with different orientations over the Co_3O_4/TiO_2-3DHS catalyst attributed to the curvature effect associated with the three-dimensional hollow structure,[16,29,30] which could facilitate the formation of active sites with three-dimensional distribution

Table 1. Effect of Co_3O_4/TiO_2 and Co_3O_4/TiO_2-3DHS on the Characteristics of the Discharge[a]

packing catalysts	input voltage (V)	input current (A)	input power (W)	discharge power (W)	Q (%)	C_{eff} (pF)	Q_{trans} (μC)
Co_3O_4/TiO_2	23	1.49	34.27	14.59	42.57	16	0.15
Co_3O_4/TiO_2-3DHS	23	1.67	38.41	18.71	48.71	24	0.22

[a]Q = output efficiency of power supplies; C_{eff} = effective capacitance; and Q_{trans} = quantity of transferred charge.

characteristics. Additionally, the elemental distribution of Ti, O, and Co within the nanoreactors is shown in Figure S4 (Supporting Information), respectively. The EDS mapping results revealed that Co and O species uniformly distributed on the two catalysts.

3.2. Surface Species. The XPS spectra were used to analyze the chemical states of Co, O, and Ti over the surface of Co_3O_4/TiO_2 and Co_3O_4/TiO_2-3DHS catalysts. The Co 2p XPS spectrum of the two different catalysts (Figure 3a) was further split into six conspicuous peaks of Co^{2+} $2p_{3/2}$ (782.1/782.4 eV), Co^{2+} $2p_{1/2}$ (796.6/796.7 eV), Co^{3+} $2p_{3/2}$ (779.9/780.0 eV), Co^{3+} $2p_{1/2}$ (795.1/795.3 eV), and the satellite peaks (802.0/802.1 eV), respectively, which were in good agreement with the presence of Co_3O_4.[31,32] Calculations confirmed that the Co^{2+} concentration in Co_3O_4/TiO_2-3DHS (37.9%) was higher than that in Co_3O_4/TiO_2 (36.1%). It was clear that Co^{2+} is significantly important for catalytic oxidation. Figure 3b shows the O 1s XPS spectra of Co_3O_4/TiO_2 and Co_3O_4/TiO_2-3DHS catalysts are deconvoluted into two peaks, which are in good accord with surface lattice oxygen (529.0/529.2 eV), denoted as O_β and chemisorbed oxygen (530.6/530.7 eV), denoted as O_α.[33,34] The ratio of O_α/O_{total} in Co_3O_4/TiO_2-3DHS (23.9%) was higher than that in Co_3O_4/TiO_2 (15.7%). It is well known that surface chemisorbed oxygen plays a crucial role in the oxidation reaction.[14] We speculate that the hydrothermal method produces more coordination-unsaturated chemical bonds on the surface of the catalyst, increasing the content of the chemisorbed oxygen and $Co^{2+}/(Co^{2+} + Co^{3+})$.[6] Figure 3c shows the peaks at 457.8−457.9 and 463.5−463.6 eV in two catalysts, which could be attributed to Ti $2p_{3/2}$ and Ti $2p_{1/2}$, respectively, in good agreement with the presence of TiO_2.[31] The Co atomic ratios of Co_3O_4/TiO_2 and Co_3O_4/TiO_2-3DHS were 3.9 and 3.2%, respectively.

3.3. Plasma-Catalytic Process. *3.3.1. Plasma-Catalytic Performance Assessment.* The above experimental results show that we have successfully constructed a three-dimensional hollow structure in Co_3O_4/TiO_2-3DHS. To verify the superiority of this structure, two kinds of catalysts with different structures were placed in the DBD reactor, and the experiments of plasma-catalytic oxidation of NO were carried out. There was a significant difference in the NO oxidation efficiency, as shown in Figure 4a. Strikingly, the results plotted in Figure 4b showed that the Co_3O_4/TiO_2-3DHS catalyst exhibits excellent activity toward NO oxidation (almost 100%) at low V_{P-P} (21−25 kV) in the absence of SO_2 and H_2O, far surpassing Co_3O_4/TiO_2 catalyst.

To explore the synergistic effect between catalyst and plasma, the Q-U Lissajous figures with two different catalysts are shown in Figure S5 at a constant input voltage of 23 kV. The effective capacitance (C_{eff}) for Co_3O_4/TiO_2-3DHS (24 pF) was higher than Co_3O_4/TiO_2 (16 pF) (Table 1). Furthermore, the quantity of transferred charge increased in the following sequence: Co_3O_4/TiO_2-3DHS (0.22 μC) > Co_3O_4/TiO_2 (0.15 μC). This indicated that packing Co_3O_4/TiO_2-3DHS catalyst in the discharge region produced more energetic electrons.[21] Especially, the discharge power and

output efficiency of power supplies were further increased when the Co_3O_4/TiO_2-3DHS catalyst was packed in the reactor, suggesting that a three-dimensional hollow structure facilitates the charge accumulation.[22]

These results demonstrated that the three-dimensional hollow nanoreactor might be easier to produce a synergistic effect with the plasma reactor. The enhancement of the charge transfer and the generation of more energetic electrons can effectively accelerate the reactions in the plasma-catalytic process. Hence, eqs 5 and 6 may occur more rapidly on the Co_3O_4/TiO_2-3DHS catalyst surface.[6,13]

$$NO + O^* \rightarrow NO_2 \tag{5}$$

$$NO + O_3 \rightarrow NO_2 + O_2 \tag{6}$$

When the catalyst is used in an actual industrial flue gas, the SO_2 tolerance of the catalyst must be evaluated because the coexistence of SO_2 may be detrimental to the catalyst. To this end, we designed a comparative experiment, and the effect of SO_2 on the oxidation efficiency of NO was investigated. As summarized in Figure 4c, the addition of SO_2 led to a decrease in the NO oxidation efficiency at 21 kV over the two catalysts. Surprisingly, the NO oxidation efficiency of Co_3O_4/TiO_2-3DHS reached almost 100% when the voltage was slightly increased to 25 kV, indicating that the effect of SO_2 on the catalytic activity of Co_3O_4/TiO_2-3DHS was negligible. However, in the same case, the oxidation efficiency corresponding to Co_3O_4/TiO_2 is only ∼70%, indicating that the coexistence of SO_2 in flue gas has a significant impact on NO oxidation. Compared with the Co_3O_4/TiO_2 catalyst, Co_3O_4/TiO_2-3DHS has lower conversion efficiency for SO_2 (∼30%), based on which it is speculated that the reaction rates corresponding to eqs 7 and 8 are much lower than those on the surface of Co_3O_4/TiO_2. Given SO_3 is a strong acidic gas and a major source of the corrosion of the pipe wall,[20] it is reasonably expected that Co_3O_4/TiO_2-3DHS can remarkably improve the anti-corrosion of NTP reactors, as confirmed by a 1-h continuous test, as shown in Figure S6 (Supporting Information). Given that both present the same Co_3O_4 catalysts, we can speculate that the excellent sulfur resistance of Co_3O_4/TiO_2-3DHS is mainly attributed to its unique three-dimensional hollow structure. This structure may change the selective adsorption of SO_2 and NO, which has been supported by DFT calculations below. In addition, the conversion efficiency of SO_2 is lower than that of NO in the given V_{P-P} range, which is directly related to the fact that the reaction rate constants of NO with O^* and O_3 are much higher than those of SO_2 with O^* and O_3.[15,35]

$$SO_2 + O^* \rightarrow SO_3 \tag{7}$$

$$SO_2 + O_3 \rightarrow SO_3 + O_2 \tag{8}$$

Figure 4d evaluates the catalytic oxidation efficiency of NO under the coexistence of SO_2 and H_2O. It is known that H_2O is usually used as a source to generate OH^* in the NTP process via eq 9.[20,36] From Figure 4d, it can be seen that the
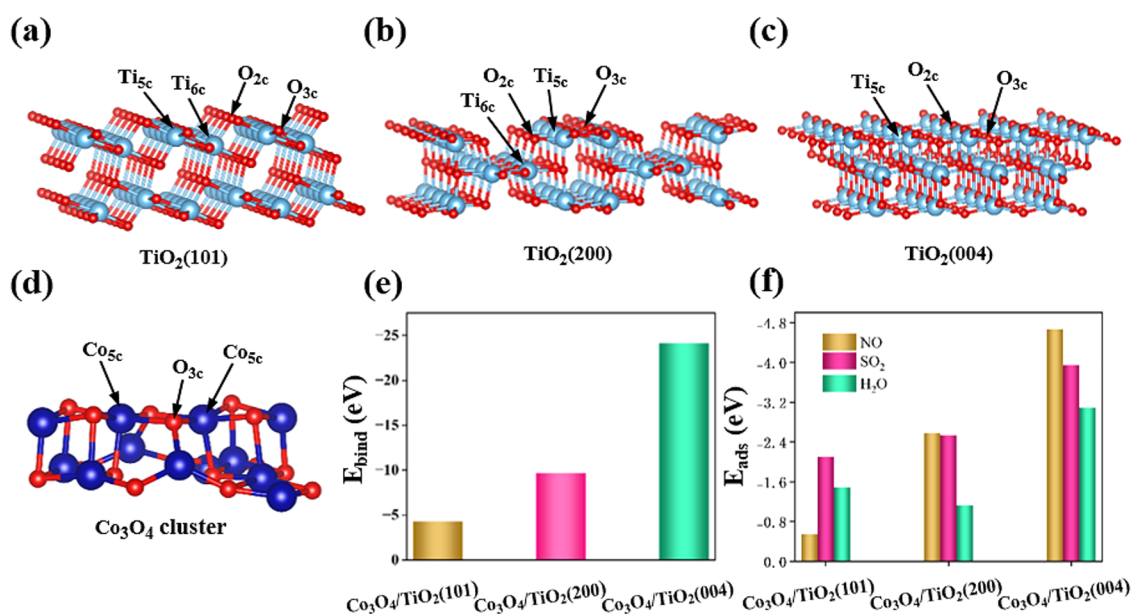
Figure 5. Geometric structures of (a) $TiO_2(101)$, (b) $TiO_2(200)$, (c) $TiO_2(004)$, and (d) Co_3O_4 cluster. (e) Binding Energy (E_{bind}) of $Co_3O_4/TiO_2(101)$, $Co_3O_4/TiO_2(200)$, and $Co_3O_4/TiO_2(004)$, respectively. (f) Adsorption energies (E_{ads}) of NO, SO_2, and H_2O over different Co sites.

incorporation of water vapor significantly reduces the catalytic activity of Co_3O_4/TiO_2 under low V_{P-P} (21−25 kV) conditions, which is consistent with our previous study.[6,15] One of the reasons is that H_2O will capture a large number of electrons, resulting in the reduction of high-energy electrons. Another reason is that H_2O will compete with NO for active sites on the catalyst surface.[2,20,36] When V_{P-P} increases from 25 to 29 kV, the discharge energy increases gradually. The more the discharge energy increases, the more free radicals (O*, OH*) are produced.[20,36] Therefore, the oxidation efficiency of NO gradually increases with the increase of V_{P-P} and reaches the highest value (91.5%) at 29 kV. When V_{P-P} increased from 29 to 31 kV, however, the oxidation efficiency decreased, mainly due to the presence of eq 10.[13] If Co_3O_4/TiO_2-3DHS is used as the catalyst, compared with Figure 4c, the NO oxidation efficiency was improved at 21 kV, which was mainly attributed to the introduction of eq 11.[36] The oxidation efficiency was almost 100% at 23 kV, which showed that the effect of H_2O on the catalytic activity of Co_3O_4/TiO_2-3DHS is also negligible.

$$H_2O + O^* \rightarrow OH^* + OH^* \tag{9}$$

$$NO_2 + O^* \rightarrow NO + O_2 \tag{10}$$

$$NO + OH^* \rightarrow HNO_2 \tag{11}$$

When SO_2 and H_2O are present in the flue gas, the conversion efficiency of Co_3O_4/TiO_2 to SO_2 gradually increases with increasing voltage, as shown in Figure 4d. It indicates that SO_2 will also be oxidized and converted due to the existence of eqs 12 and 13.[36] In contrast, the conversion efficiency of SO_2 by the Co_3O_4/TiO_2-3DHS is still low, a phenomenon similar to that of Figure 4c. We speculate that this phenomenon can be attributed to two reasons: (1) eqs 12 and 13 may be easier to occur on the surface of the Co_3O_4/TiO_2 catalyst; (2) SO_2 and H_2O may not be readily adsorbed on the surface of the Co_3O_4/TiO_2-3DHS catalyst. Based on the above comparison and analysis, we believe that Co_3O_4/TiO_2-3DHS coupled with nonthermal plasma has higher catalytic oxidation efficiency of

NO at a lower peak−peak voltage. From our previous work,[36] a lower peak−peak voltage means higher discharge efficiency. Therefore, it is speculated that the three-dimensional hollow structure can effectively reduce the discharge energy consumption of the plasma-catalytic process and maintain excellent catalytic activity. Meanwhile, the Co_3O_4/TiO_2-3DHS catalyst has more robust sulfur/water resistance, which means that it has particular advantages and great potential in the plasma-catalytic oxidation of NO. In the case of plasma without a catalyst, the highest NO oxidation and SO_2 conversion efficiency were 57.4 and 8.5%, respectively (Figure S7, Supporting Information). The results showed that the inner electrode is unreactive to NO and SO_2.

$$SO_2 + OH^* \rightarrow HOSO_2 \tag{12}$$

$$HOSO_2 + O_2 \rightarrow SO_3 + HO_2 \tag{13}$$
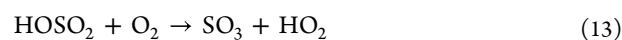
3.3.2. Stability of the Co_3O_4/TiO_2-3DHS Catalyst. To explore the stability of a three-dimensional hollow structure, we packed 0.5 g of the Co_3O_4/TiO_2-3DHS catalyst in a DBD reactor and carried out plasma-catalytic reaction experiments for up to 10 h. We chose the oxidation efficiency of NO as the index to measure the stability. As shown in Figure S8a (Supporting Information), after a long time of plasma-catalytic reaction, the oxidation efficiency is between 91.5 and 94.5%. This small change interval can show that the catalyst still has excellent stability after a long time of use. Apart from a slight change in the oxidation efficiency of NO, the XRD patterns of the fresh and spent Co_3O_4/TiO_2-3DHS catalyst (Figure S8b, Supporting Information) revealed that phase structure is well retained after 10 h. These results unambiguously illustrated that the poisoning associated with SO_2 and H_2O has been effectively inhibited on Co_3O_4/TiO_2-3DHS surfaces. Moreover, the stability of various NO oxidation catalysts is provided in Table S2 (Supporting Information). Compared with other metal oxide catalysts, Co_3O_4-TiO_2-3DHS has the best stability at long-time testing, testifying to its superior catalytic activity.

The FTIR spectra of the two catalysts before and after the reaction are presented in Figure S9 (Supporting Information).
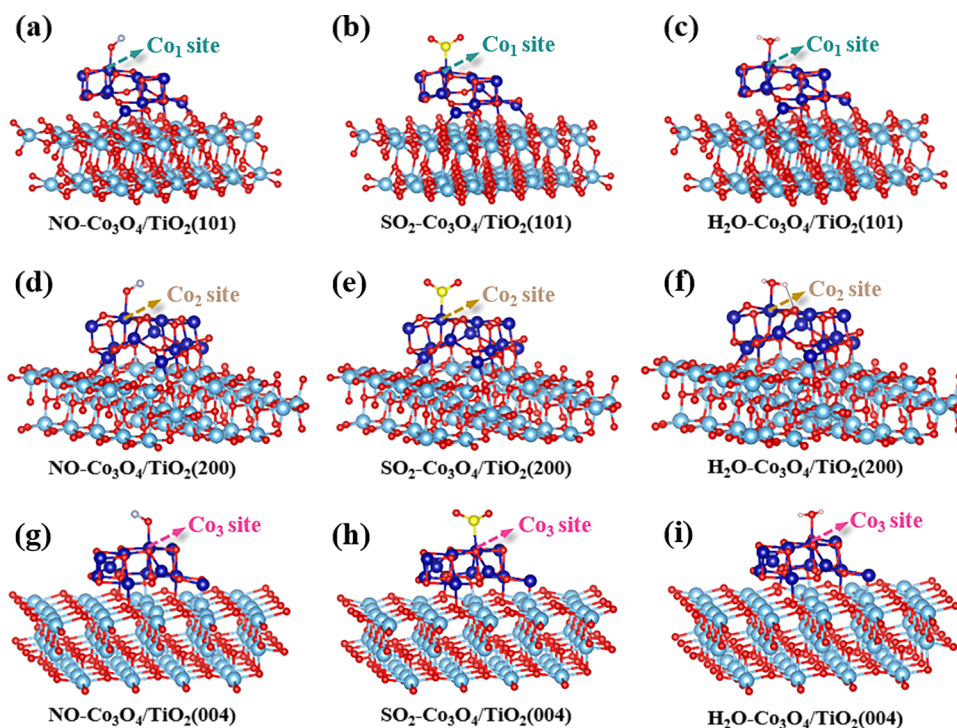
Figure 6. Adsorption configurations of NO, SO_2, and H_2O over the catalysts with three typical coordination environments, including (a–c) $Co_3O_4/TiO_2(101)$, (d–f) $Co_3O_4/TiO_2(200)$, and (g–i) $Co_3O_4/TiO_2(004)$. Ti, Co, O, H, and S are represented by light blue, navy blue, red, white, and yellow balls.

The FTIR spectra data were normalized. The spent catalysts were labeled as S-Co_3O_4/TiO_2-3DHS and S-Co_3O_4/TiO_2. The major peaks at 3386 and 1630 cm^{-1} were assigned to the hydroxyl groups stretching and bending vibration of the adsorbed water.[37−39] Notably, the peak intensity of hydroxyl groups on S-Co_3O_4/TiO_2-3DHS was weaker than that on S-Co_3O_4/TiO_2, indicating the superior water tolerance of the three-dimensional hollow structure. Two sharp peaks of the Co_3O_4/TiO_2-3DHS catalyst at 667 and 576 cm^{-1} are indicative of the Co−O vibration.[38] The surface sulfate species of S-Co_3O_4/TiO_2 were confirmed by the peaks around 1138 and 1039 cm^{-1}.[38−41] In contrast, the FTIR result of S-Co_3O_4/TiO_2-3DHS did not show a distinct peak at the above vibration frequencies, confirming the weaker adsorption intensity of the Co_3O_4/TiO_2-3DHS catalyst toward SO_2 and suggesting its superior SO_2 tolerance, as further supported by our DFT calculations below.

3.4. DFT Calculations. To achieve an advanced understanding of the high performance observed from TiO_2-3DHS, DFT calculations have been carried out, focusing on two central questions: (1) whether or not strong interfacial bonding between Co_3O_4 and TiO_2 substrate can be established, which is the basis for following catalysis mediation; and (2) how minority surfaces introduced by TiO_2-3DHS affect the selectivity of Co_3O_4 catalyst. Under such consideration, TiO_2 was modeled by a typical majority surface (101), but TiO_2-3DHS is featured with minority surfaces (200) and (004), as illustrated by HRTEM images and structure models in Figure 5. Specifically, three sites labeled as Co_1, Co_2, and Co_3, and the corresponding gas-adsorption geometries were presented for Co_3O_4/TiO_2(101), Co_3O_4/TiO_2(200), and Co_3O_4/TiO_2(004) (Figure 6). It is worth pointing out that these Co-sites are located on the surface of the Co_3O_4 cluster rather than at the interface, under which

they have the same five-coordination geometry. Based on these models, further investigation of Co_3O_4 bonding and gas adsorption has been performed.

Co_3O_4-TiO_2 bonding is the basis for following gas adsorption, which has been investigated with the loading of the Co_3O_4 cluster, with optimized geometries, as shown in Figure 5a−d. During our calculations, the same Co_3O_4 cluster was introduced to TiO_2 surfaces, followed by complete optimization. As revealed by the geometries, Co_3O_4 is fixed over TiO_2 surfaces via Co−O and Ti−O bonding, with binding energy being as high as 4−24 eV. Chemical bonding, rather than nonbonding interaction, dominates the interface. More importantly, significant difference for (101), (200), and (004) has been vividly shown by E_{bind} in Figure 5e. It is not surprising because the majority surface (101) has much lower surface energy than that of the minority surfaces (200) and (004), due to different coordination on the surface. Specifically, unsaturated Ti and O, showing as Ti_{5c} and O_{2c}, are 50% on (101), while ∼75% on (200) and 100% on (004). These unsaturated atoms prefer to bond with Co and O, as revealed by Figure 5a−c.

Now, we turn to the investigation of gas adsorption. Optimized geometries of gas (NO, SO_2, H_2O) are presented in Figure 6, and calculated adsorption energies are shown in Figure 5f. In all cases, gas has been adsorbed by five-coordinated Co. In the case of Co_3O_4/TiO_2(101), NO was weakly adsorbed with adsorption energy (−0.55 eV), which is lower than that for SO_2 (−2.10 eV) and H_2O (−1.48 eV) adsorption, indicating poor selectivity for NO oxidation. However, such a situation can be notably improved when Co_3O_4 is loaded to TiO_2(200) and (004), especially the latter showing a reversed capacity: NO adsorption becomes more favorable than SO_2 and H_2O, as indicated by the adsorption energy. Specifically, the order of the adsorption energies of the
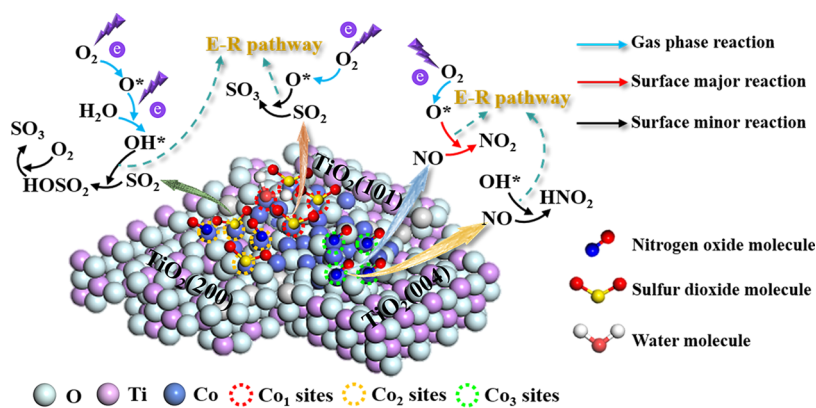
Figure 7. Proposed mechanism of the Co$_3$O$_4$/TiO$_2$-3DHS catalyst surface.

three gases on the Co$_3$ sites is ranked as NO-Co$_3$ > SO$_2$- Co$_3$ > H$_2$O- Co$_3$. This result indicates that the Co$_3$ site preferentially adsorbs NO, which may ensure that SO$_2$ and H$_2$O do not easily poison the catalyst. The above DFT simulation results show that NO can be readily adsorbed on the surfaces of Co$_3$O$_4$/TiO$_2$(200) and Co$_3$O$_4$/TiO$_2$(004), while SO$_2$ and H$_2$O are favorably adsorbed on the surfaces of Co$_3$O$_4$/TiO$_2$(101) and Co$_3$O$_4$/TiO$_2$(200).

The above understanding is of great significance for the design of catalysts in the context of efficient oxidation of NO. Combined with the experimental phenomena in Section 3.3 and the DFT simulation results in this section, we can reasonably infer that (1) the poor sulfur and water tolerance of the Co$_3$O$_4$/TiO$_2$ catalyst is due to the fact that the active sites in the catalyst are mainly Co$_1$ sites, and (2) Co$_3$O$_4$/TiO$_2$-3DHS has three different types of active sites (Co$_1$, Co$_2$, and Co$_3$ sites), contributing to the formation of different flue gas enrichment regions on the surface of the catalysts, which may enhance the SO$_2$ and H$_2$O tolerance.

3.5. Mechanism of the Plasma-Catalytic Process. As reflected in eqs 5 and 11, free radicals (O* and OH*) are actively involved in the reaction. O* mainly originates from the plasma discharge via O$_3$ decomposition, which reacts with water to release OH* species in the flue gas. Based on the results of numerous studies,[42−44] we speculate that the plasma-catalytic oxidation of NO and SO$_2$ by O* and OH* in collaboration with Co$_3$O$_4$/TiO$_2$-3DHS mainly follows the Eley−Rideal (E−R) reaction mechanism. According to DFT calculations, the catalytic oxidation of NO occurs primarily on the surface of Co$_3$O$_4$/TiO$_2$(004) and secondarily on the surface of Co$_3$O$_4$/TiO$_2$(200). The catalytic oxidation of SO$_2$ mainly occurred on the surface of Co$_3$O$_4$/TiO$_2$(101), followed by Co$_3$O$_4$/TiO$_2$(200). The above understanding has been summarized into the reaction pathways in Figure 7. With reference to Figure 7,[1,43,44] we can describe the course of the reaction in general. During the oxidation of NO, most of the NO molecules can be adsorbed on the Co$_3$ site, and then O* attacks the NO molecules to form NO$_2$ molecules which can be desorbed from the catalyst surface. At the same time, it mainly reacts with O* to produce OH* in the gas phase because H$_2$O adsorption is not energetically favorable for NO on the surface of Co$_3$O$_4$/TiO$_2$-3DHS. Consequently, OH* attacks the adsorbed NO molecules to form HNO$_2$. Because the reaction rate of OH* with NO is much lower than that of O*, the reaction involving O* is the surface major elementary step for NO oxidation, while the reaction involving OH* is the

minor one. During the oxidation of SO$_2$, most of the SO$_2$ molecules can be adsorbed on Co$_1$ sites. O* attacks the adsorbed SO$_2$ molecules to form SO$_3$ molecules, which are then desorbed from the catalyst surface. SO$_2$ can also react with OH* to form HOSO$_2$, which then reacts with O$_2$ to produce SO$_3$ and eventually desorbs from the catalyst surface. Because the reaction rate of NO is higher than that of SO$_2$,[14] the catalytic reaction of SO$_2$ is also a surface minor reaction.

4. CONCLUSIONS

In this work, we tried to convert NO in flue gas based on the technical route of plasma-catalytic oxidation rather than SCR. Co oxide was selected from many transition-metal oxides, and two kinds of catalysts, Co$_3$O$_4$/TiO$_2$ and Co$_3$O$_4$/TiO$_2$-3DHS, were synthesized by wet impregnation and hydrothermal methods. Combined with the method of nonthermal plasma, we verified the oxidation efficiency of NO in the presence of SO$_2$ and H$_2$O through experiments and inferred the reaction mechanism and route with the help of experimental phenomena and DFT simulation results. Studies have shown the following. By integrating the coupled DBD reactor and the three-dimensional hollow structure catalyst (Co$_3$O$_4$/TiO$_2$-3DHS), higher efficiency (almost 100%) and more excellent stability (10 h) of NO oxidation were obtained under the concentration of NO (160 ppm), SO$_2$ (400 ppm), H$_2$O (5 vol %), and O$_2$ (6 vol %) at low V_{P-P} (21−25 kV). The improvement of the performance of plasma-catalytic oxidation of NO caused by the 3D hollow nanoreactor can be attributed to the unique cluster-support effect, mediating the distribution of the active sites on the catalyst surface, driving the selective adsorption of NO, SO$_2$, and H$_2$O, weakening the poisoning effect of SO$_2$ and H$_2$O, thereby improving the catalytic activity. This work is expected to provide a broader theoretical insight into the technical route of the Co$_3$O$_4$/TiO$_2$-3DHS catalyst coupled plasma-catalytic oxidation of NO in flue gas and show the potential advantages of a three-dimensional hollow nanoreactor in a plasma-catalytic system. In the future, this plasma-catalytic process combined with a wet scrubber adsorbing process and a membrane system will convert NO$_2$ into high-value products that can be further used in the production of complex fertilizers, thus realizing the resource utilization of nitrogen oxides.

ASSOCIATED CONTENT

Supporting Information

The Supporting Information is available free of charge at https://pubs.acs.org/doi/10.1021/acsomega.3c02132.

Preparation of Co_3O_4/TiO_2 catalyst; textural and chemical properties of the fresh catalysts; the stability of various NO oxidation catalysts; NO oxidation efficiency of MO_X/TiO_2 and MO_X/TiO_2-3DHS (M = Fe, Co, Ni) in the plasma-catalytic reaction; schematic diagram of the DBD plasma-catalytic reactor; optimized structures of three slab models; EDS mapping of Co_3O_4/TiO_2 and Co_3O_4/TiO_2-3DHS; rubber hose corrosion image after plasma-catalytic reaction; NO oxidation and SO_2 conversion efficiency under plasma-only conditions with SO_2 and H_2O; XRD patterns of fresh and spent Co_3O_4/TiO_2-3DHS catalysts; and time-on stream stability of the oxidation of NO over the Co_3O_4/TiO_2-3DHS catalyst (PDF)

AUTHOR INFORMATION

Corresponding Author

Dong Fu − *Hebei Key Lab of Power Plant Flue Gas Multi-Pollutants Control, Department of Environmental Science and Engineering, North China Electric Power University, Baoding 071003, P. R. China; MOE Key Laboratory of Resources and Environmental Systems Optimization, North China Electric Power University, Beijing 102206, P. R. China;* orcid.org/0000-0002-8553-8680; Email: fudong@tsinghua.org.cn

Authors

Yujie Liao − *Hebei Key Lab of Power Plant Flue Gas Multi-Pollutants Control, Department of Environmental Science and Engineering, North China Electric Power University, Baoding 071003, P. R. China; MOE Key Laboratory of Resources and Environmental Systems Optimization, North China Electric Power University, Beijing 102206, P. R. China*

Kun Zhao − *Hebei Key Lab of Power Plant Flue Gas Multi-Pollutants Control, Department of Environmental Science and Engineering, North China Electric Power University, Baoding 071003, P. R. China; MOE Key Laboratory of Resources and Environmental Systems Optimization, North China Electric Power University, Beijing 102206, P. R. China*

Ke Chen − *Hebei Key Lab of Power Plant Flue Gas Multi-Pollutants Control, Department of Environmental Science and Engineering, North China Electric Power University, Baoding 071003, P. R. China; MOE Key Laboratory of Resources and Environmental Systems Optimization, North China Electric Power University, Beijing 102206, P. R. China*

Chenghua Sun − *Department of Chemistry and Biology, Swinburne University of Technology, Hawthorn, Victoria 3122, Australia;* orcid.org/0000-0001-7654-669X

Complete contact information is available at:
https://pubs.acs.org/10.1021/acsomega.3c02132

Author Contributions

Y.L.: Conceptualization, methodology, investigation, validation, formal analysis, data curation, and writing—original draft. K.Z.: Methodology, investigation, and formal analysis. K.C.: Methodology and investigation. C.S.: Methodology and investigation. D.F.: Supervision, funding acquisition, and writing—review and editing.

Notes

The authors declare no competing financial interest.

REFERENCES

(1) Yang, W.; Liu, X.; Chen, X.; Cao, Y.; Cui, S.; Jiao, L.; Wu, C.; Chen, C.; Fu, D.; Gates, I. D.; et al. A Sulfur-Tolerant MOF-Based Single-Atom Fe Catalyst for Efficient Oxidation of NO and Hg^0. *Adv. Mater.* **2022**, *34*, No. e2110123.

(2) Xiong, S.; Peng, Y.; Wang, D.; Huang, N.; Zhang, Q.; Yang, S.; Chen, J.; Li, J. The role of the Cu dopant on a Mn_3O_4 spinel SCR catalyst: Improvement of low-temperature activity and sulfur resistance. *Chem. Eng. J.* **2020**, *387*, No. 124090.

(3) Li, X.; Wang, Z.; Shi, H.; Dai, D.; Zuo, S.; Yao, C.; Ni, C. Full spectrum driven SCR removal of NO over hierarchical $CeVO_4/$ attapulgite nanocomposite with high resistance to SO_2 and H_2O. *J. Hazard. Mater.* **2020**, *386*, No. 121977.

(4) Xiao, M.; Yang, X.; Peng, Y.; Guo, Y.; Wei, Y.; Ge, M.; Yu, X. Confining shell-sandwiched Ag clusters in MnO_2-CeO_2 hollow spheres to boost activity and stability of toluene combustion. *Nano Res.* **2022**, *15*, 7042−7051.

(5) Hao, R.; Yang, S.; Yuan, B.; Zhao, Y. Simultaneous desulfurization and denitrification through an integrative process utilizing $NaClO_2/Na_2S_2O_8$. *Fuel. Process. Technol.* **2017**, *159*, 145−152.

(6) Liao, Y.; Zhao, K.; Yang, J.; An, X.; Zhang, P.; Dou, Y.; Zhao, M.; Fu, D. Hetero-Shelled Hollow Structure Coupled with Non-Thermal Plasma Inducing Spatial Charge Rearrangement for Superior NO Conversion and Sulfur Resistance. *Small* **2022**, *18*, No. e2106680.

(7) Wang, D.; Cheng, J.; Wang, B.; Lou, J.; Li, Y.; Li, X.; Li, Z.; Liu, X.; Meng, Q.; Gao, P.; An, J. Plasma-catalytic high-efficiency oxidation of NO over Co-Mn/Ti catalysts using surface dielectric barrier discharge plasma. *Vacuum* **2019**, *167*, 249−254.

(8) Wang, J.; Yi, H.; Tang, X.; Zhao, S.; Gao, F.; Yang, Z. Oxygen plasma-catalytic conversion of NO over MnOx: Formation and reactivity of adsorbed oxygen. *Catal. Commun.* **2017**, *100*, 227−231.

(9) Zhang, Y.; Zhu, M.; Wei, Q.; Wang, M. Removing Chlorobenzene via the Synergistic Effects of Adsorption and Catalytic Oxidation over Activated Carbon Fiber Loaded with Transition Metal Oxides. *Atmosphere* **2022**, *13*, No. 2074.

(10) Wang, Q.; Yang, J.; Liu, Z.; Wen, Y.; Chen, R.; Shan, B. A first-principles based microkinetic study of $ZnMn_{1.5}TM_{0.5}O_4$ (TM = 3d transition metal) for NO oxidation. *Appl. Surf. Sci.* **2022**, *600*, No. 154069.

(11) Ren, H.; Yu, R.; Wang, J.; Jin, Q.; Yang, M.; Mao, D.; Kisailus, D.; Zhao, H.; Wang, D. Multishelled TiO_2 hollow microspheres as anodes with superior reversible capacity for lithium ion batteries. *Nano. Lett.* **2014**, *14*, 6679−6684.

(12) Liu, L.; Zheng, C.; Chen, J.; Zhou, J.; Gao, X.; Ni, M.; Cen, K. Plasma-induced adsorption of elemental mercury on TiO_2 supported metal oxide catalyst at low temperatures. *Fuel. Process. Technol.* **2015**, *138*, 14−20.

(13) Wang, J.; Yi, H.; Tang, X. Non-thermal plasma-assisted catalytic oxidation of NO in a dielectric barrier discharge reactor packed with MO_x/Al_2O_3 (M = Mn or Co) as catalysts. *J. Chem. Technol. Biotechnol.* **2019**, *94*, 3180−3189.

(14) Cui, S.; Hao, R.; Fu, D. Integrated method of non-thermal plasma combined with catalytical oxidation for simultaneous removal of SO_2 and NO. *Fuel* **2019**, *246*, 365−374.

(15) Cui, S.; Zhong, Z.; Liao, Y.; Qi, L.; Fu, D. Simultaneous Removal of NO and SO_2 via an Integrated System of Nonthermal Plasma Combined with Catalytic Oxidation and Wet Electrostatic Precipitator. *Energy Fuels* **2019**, *33*, 10078−10089.

(16) Yu, Z.; Ji, N.; Xiong, J.; Li, X.; Zhang, R.; Zhang, L.; Lu, X. Ruthenium-Nanoparticle-Loaded Hollow Carbon Spheres as Nanoreactors for Hydrogenation of Levulinic Acid: Explicitly Recognizing the Void-Confinement Effect. *Angew. Chem., Int. Ed.* **2021**, *60*, 20786−20794.

(17) Hu, Z.; Li, X.; Zhang, S.; Li, Q.; Fan, J.; Qu, X.; Lv, K. Fe_1/TiO_2 Hollow Microspheres: Fe and Ti Dual Active Sites Boosting the Photocatalytic Oxidation of NO. *Small* **2020**, *16*, No. e2004583.

(18) She, P.; Qin, J. S.; Sheng, J.; Qi, Y.; Rui, H.; Zhang, W.; Ge, X.; Lu, G.; Song, X.; Rao, H. Dual-Functional Photocatalysis for Cooperative Hydrogen Evolution and Benzylamine Oxidation Coupling over Sandwiched-Like $Pd@TiO_2@ZnIn_2S_4$ Nanobox. *Small* **2022**, *18*, No. e2105114.

(19) Waqas, M.; Wei, Y.; Mao, D.; Qi, J.; Yang, Y.; Wang, B.; Wang, D. Multi-shelled TiO_2/Fe_2TiO_5 heterostructured hollow microspheres for enhanced solar water oxidation. *Nano Res.* **2017**, *10*, 3920−3928.

(20) Cui, S.; Liao, Y.; Gao, Z.; Fu, D. Dielectric barrier discharge coupling catalytic oxidation for efficient conversion of Hg^0 from flue gas. *Fuel* **2021**, *287*, No. 119521.

(21) Wang, Y.; Chen, Y.; Harding, J.; He, H.; Bogaerts, A.; Tu, X. Catalyst-free single-step plasma reforming of CH_4 and CO_2 to higher value oxygenates under ambient conditions. *Chem. Eng. J.* **2022**, *450*, No. 137860.

(22) Diao, Y.; Zhang, X.; Liu, Y.; Chen, B.; Wu, G.; Shi, C. Plasma-assisted dry reforming of methane over Mo_2C-Ni/Al_2O_3 catalysts: Effects of β-Mo_2C promoter. *Appl. Catal. B.* **2022**, *301*, No. 120779.

(23) Fang, Q.; Zhu, B.; Sun, Y.; Song, W.; Xu, M. Effects of alkali metal poisoning and cobalt modification on the NH_3 adsorption behavior on the Mn_xO_y/Ni (1 1 1) surface: A DFT-D study. *Appl. Surf. Sci.* **2020**, *509*, No. 144901.

(24) Zhao, Z.; Liu, Q. Effects of lanthanide doping on electronic structures and optical properties of anatase TiO_2 from density functional theory calculations. *J. Phys. D: Appl. Phys.* **2008**, *41*, No. 085417.

(25) Lee, A. T.; Ismail-Beigi, S. Magnetism of (La-$CoO_3)_n$+(LaTiO_3)_n$ superlattices (n = 1, 2). *Phys. Rev. B* **2020**, *101*, No. 144423.

(26) Piskorz, W.; Zasada, F.; Wojtowicz, G.; Morawski, A.; Macyk, W.; Sojka, Z. Attaching titania clusters of various size to reduced graphene oxide and its impact on the conceivable photocatalytic behavior of the junctions-a DFT/D + U and TD DFTB modeling. *J. Phys.: Condens. Mater.* **2019**, *31*, No. 404001.

(27) Li, H.; Liu, S.; Yang, J.; Liu, Y.; Hu, Y.; Feng, S.; Yang, Z.; Zhao, J.; Qu, W. Role of SO_2 and H_2O in the mercury adsorption on ceria surface: A DFT study. *Fuel* **2020**, *260*, No. 116289.

(28) Zhu, T.; Liu, K.; Wang, H.; Wang, J.; Li, F.; Wang, C.; Song, H. Comparative study of hydrodeoxygenation performance over Ni and Ni_2P catalysts for upgrading of lignin-derived phenolic compound. *Fuel* **2023**, *331*, No. 125663.

(29) Xiao, S.; Li, Z.; Liu, J.; Song, Y.; Li, T.; Xiang, Y.; Chen, J. S.; Yan, Q. SeC Bonding Promoting Fast and Durable Na^+ Storage in Yolk-Shell $SnSe_2@Se$-C. *Small* **2020**, *16*, No. e2002486.

(30) Wei, Y.; Yang, N.; Huang, K.; Wan, J.; You, F.; Yu, R.; Feng, S.; Wang, D. Steering Hollow Multishelled Structures in Photocatalysis: Optimizing Surface and Mass Transport. *Adv. Mater.* **2020**, *32*, No. e2002556.

(31) Yao, X.; Wang, X.; Sun, L.; Li, L.; Kan, E.; Ouyang, B.; Zhang, W. Popcorn-like Co_3O_4 nanoparticles confined in a three-dimensional hierarchical N-doped carbon nanotube network as a highly-efficient trifunctional electrocatalyst for zinc−air batteries and water splitting devices. *Inorg. Chem. Front.* **2022**, *9*, 2517−2529.

(32) Bai, S.; Tian, K.; Tian, Y.; Guo, J.; Feng, Y.; Luo, R.; Li, D.; Chen, A.; Liu, C. C. Synthesis of Co_3O_4/TiO_2 composite by pyrolyzing ZIF-67 for detection of xylene. *Appl. Surf. Sci.* **2018**, *435*, 384−392.

(33) Zhao, B.; Yi, H.; Tang, X.; Li, Q.; Liu, D.; Gao, F. Using CuO-MnO_x/AC-H as catalyst for simultaneous removal of Hg degrees and NO from coal-fired flue gas. *J. Hazard. Mater.* **2019**, *364*, 700−709.

(34) Zhang, T.; Liu, J.; Wang, D.; Zhao, Z.; Wei, Y.; Cheng, K.; Jiang, G.; Duan, A. Selective catalytic reduction of NO with NH_3 over HZSM-5-supported Fe−Cu nanocomposite catalysts: The Fe−Cu bimetallic effect. *Appl. Catal., B* **2014**, *148−149*, 520−531.

(35) Jõgi, I.; Levoll, E.; Raud, J. Plasma oxidation of NO in O_2:N_2 mixtures: The importance of back-reaction. *Chem. Eng. J.* **2016**, *301*, 149−157.

(36) Cui, S.; Hao, R.; Fu, D. An integrated system of dielectric barrier discharge combined with wet electrostatic precipitator for simultaneous removal of NO and SO_2: Key factors assessments, products analysis and mechanism. *Fuel* **2018**, *221*, 12−20.

(37) Zhang, L.; Qu, H.; Du, T.; Ma, W.; Zhong, Q. H_2O and SO_2 tolerance, activity and reaction mechanism of sulfated Ni−Ce−La composite oxide nanocrystals in NH_3-SCR. *Chem. Eng. J.* **2016**, *296*, 122−131.

(38) Zhang, Y.; Zhao, L.; Kang, M.; Chen, Z.; Gao, S.; Hao, H. Insights into high CO-SCR performance of CuCoAlO catalysts derived from LDH/MOFs composites and study of H_2O/SO_2 and alkali metal resistance. *Chem. Eng. J.* **2021**, *426*, No. 131873.

(39) Baylet, A.; Capdeillayre, C.; Retailleau, L.; Vernoux, P.; Figueras, F.; Giroir-Fendler, A. Relation between partial propene oxidation, sulphate content and selective catalytic reduction of NO_x by propene on ceria/sulphated titania. *Appl. Catal. B.* **2010**, *96*, 434−440.

(40) Ma, S.; Bie, X.; Gong, C.; Qu, B.; Liu, D. Scale-up experiments of SO_2 removal and the promoting behavior of NO in moving beds at medium temperatures. *Rsc. Adv.* **2021**, *11*, 8846−8856.

(41) Ju, F.; Wu, C.; Luan, H.; Tang, Z.; Pan, H.; Pan, H.; Xiu, G.; Ling, H. Influence of wet flue gas desulfurization on the pollutants monitoring in FCC flue gas. *Environ. Sci. Pollut. Res.* **2021**, *28*, 55502−55510.

(42) Zhao, S.; Shi, J.-W.; Niu, C.; Wang, B.; He, C.; Liu, W.; Xiao, L.; Ma, D.; Wang, H.; Cheng, Y. $FeVO_4$-supported Mn−Ce oxides for the low temperature selective catalytic reduction of NO_x by NH_3. *Catal. Sci. Technol.* **2021**, *11*, 6770−6781.

(43) Wang, H.; Bao, Y.; Mao, Z.; Pan, J.; Bian, H.; Xu, Z.; Lu, J.; Li, Y. Y. Supervariate Ceramics: Gelatinous and Monolithic Ceramics Fabricated under Ambient Conditions. *Adv. Eng. Mater.* **2021**, *23*, No. 2100866.

(44) Cao, J.; Liu, W.; Kang, K.; Chen, L.; Qiao, X.; Yao, X. Effects of the morphology and crystal-plane of TiO_2 on NH_3-SCR performance and K tolerance of V_2O_5-WO_3/TiO_2 catalyst. *Appl. Catal., A* **2021**, *623*, No. 118285.